ADVANCED FUNCTIONAL MATERIALS
www.afm-journal.de

Encapsulation of Nanoparticle Organic Hybrid Materials within Electrospun Hydrophobic Polymer/Ceramic Fibers for Enhanced CO_2 Capture

Kyle D. Kersey, Gahyun Annie Lee, Jeffrey H. Xu, Michelle K. Kidder, Ah-Hyung A. Park,* and Yong Lak Joo**

Liquid-like nanoparticle organic hybrid materials (NOHMs) consisting of a silica core with ionically grafted branched polyethyleneimine chains (referred to as NIPEI) are encapsulated within submicron-scale polyacrylonitrile (PAN)/polymer-derived-ceramic electrospun fibers. The addition of a room-temperature curable, liquid-phase organopolysilazane (OPSZ) ceramic precursor to the PAN/NOHM solution enhances the internal dispersion of NOHMs and forms a thin ceramic sheath layer on the fiber exterior, shielding the hydrophilic NIPEI to produce near-superhydrophobic non-woven fiber mats with contact angles exceeding 140°. 60:40 loadings of NOHMs to PAN/OPSZ can be reliably achieved with low OPSZ percentages required, and up to 4:1 NOHM:polymer loadings are possible before losing hydrophobicity. These fibers demonstrate up to ≈2 mmol CO_2 g^{-1} fiber capture capacities in a pure CO_2 atmosphere through the nonwoven fibrous networks and the permeability of the OPSZ shell. The hybrid fibers additionally show enhanced capture kinetics under pure CO_2 and 400 ppm CO_2 conditions, indicating their promising application as a direct air capture platform.

1. Introduction

With the growing emphasis on climate change and decarbonization, the development of easily scalable techniques to remove atmospheric carbon dioxide is of vital importance to slow planetary greenhouse warming, an imperative heavily underscored by the recent release of the sixth Intergovernmental Panel on Climate Change Assessment Report.[1] Carbon capture and sequestration technologies are an attainable solution while renewable energy generation and storage mature to the point of replacing fossil fuel use, though issues of scalability prevent widespread adoption on the mega- to gigaton scale of CO_2 removal. While many technologies are under development to take advantage of high-concentration sources of carbon emissions from existing sources (e.g., flue gases) using liquid-phase amine solutions, solid-supported amines, zeolites, and carbon nanotubes;[2–12] metal-organic frameworks;[13] alkali metal bases;[14–16] pressure/temperature-swing adsorption processes;[17–20] etc., ambient-air sequestration remains the greater challenge. The low concentration of CO_2 relative to other gases requires the processing of extremely large volumes of air to remove appreciable amounts of CO_2, which is highly energy intensive.

Additionally, the sorbent material must exhibit excellent selectivity toward carbon dioxide. Amine-based sorbents are perhaps widely used chemisorption capture agents due to the excellent Lewis acid-base reactivity with carbon dioxide, forming an ammonium carbamate (in dry conditions) and/or ammonium bi-

K. D. Kersey, Y. L. Joo
Robert Frederick Smith School of Chemical and Biomolecular Engineering
Department of Chemical and Biomolecular Engineering
Cornell University
Ithaca, NY 14853, USA
E-mail: ylj2@cornell.edu

G. A. Lee
Department of Chemical Engineering
Lenfest Center for Sustainable Energy
Columbia University New York
Columbia, NY 10027, USA

The ORCID identification number(s) for the author(s) of this article can be found under https://doi.org/10.1002/adfm.202301649

DOI: 10.1002/adfm.202301649

J. H. Xu
Department of Earth and Environmental Engineering & Department of Chemical Engineering
Lenfest Center for Sustainable Energy
Columbia University New York
Columbia, NY 10027, USA

M. K. Kidder
Energy Science and Technology Directorate
Oak Ridge National Laboratory
Oak Ridge, TN 37831, USA
E-mail: kidderm@ornl.gov

A.-H. A. Park
Department of Earth and Environmental Engineering & Department of Chemical Engineering
Lenfest Center for Sustainable Energy
Columbia University New York
Columbia, NY 10027, USA
E-mail: ap2622@columbia.edu

carbonate (in wet conditions) to chemically bind CO_2.[2,21–26] Regeneration is then achieved by raising the temperature of the absorbent, typically above 100 °C to decompose the carbamate back to amine, liberating an equivalent of CO_2 in the process. However, the hygroscopic or solution-phase nature of many amine sorbents requires considerable energy to disrupt the strong hydrogen bonding network during regeneration.[27] Additionally, amine sorbents tend to suffer from thermal and/or oxidative degradation at regeneration temperatures, with primary amines (the most reactive to CO_2) being the most susceptible.[28–41] Herein lie two crucial design criteria precluding the adoption of a carbon capture solution: the technology must be able to selectively reject water to avoid forming these intermolecular hydrogen bonds, and the pressure drop through the adsorbent must be minimal while still maintaining high amine densities for efficient capture.

Nanoparticle Organic Hybrid Materials (NOHMs) feature a nanometer-scale core[42] (most often SiO_2,[43–49] though examples of γ-Fe_2O_3,[50,51] ZnO,[52] TiO_2,[53] platinum,[54] gold,[54] palladium,[54] and rhodium[54] have been reported) with a polymeric corona grafted either by ionic or covalent linkages.[55] This work makes use of NOHMs consisting of a silica core with ionically grafted branched polyethyleneimine (PEI), NOHM-I-PEI (referred to as NIPEI thereinafter), where an $O^-{}^+NH_3$ ionic (I) linkage tethers the branched polyethyleneimine (PEI, M_w = 2 kDa) to a 7 nm SiO_2 core. The primary and secondary amine groups within the PEI canopy provide a high density of sites for CO_2 adsorption while the oxide core provides additional structural and thermal stability to the system due to a compacted polymer structure and internal PEI crosslinking at elevated temperatures, therefore resulting in a greater temperature of degradation.[47] Additionally, CO_2-induced structural ordering of the polymeric canopy provides an entropic driving force for binding, along with the enthalpic interactions with polyethyleneimine.[56] However, NIPEI's practical ability to capture CO_2 without a supporting matrix is considerably limited due to the high viscosity of the bulk material. The formation of a passivating carbamate skin layer on the surface of NIPEI, along with the transport limitations through the bulk medium, prevents adequate permeability of CO_2 through NIPEI.[57] The hydrophilicity of NIPEI also easily traps water, increasing the regeneration penalty.

We sought to remedy these issues by dispersing and encapsulating the bulk NIPEI in a hydrophobic fiber matrix. Gas-assisted electrospinning (**Figure 1**) provides a highly tuneable platform to fabricate sub-micron fibers from solution by synergistically combining an electric field and high-speed air.[58–62] In this work, we report the development of micron-scale composite polyacrylonitrile(PAN)/ceramic/NIPEI electrospun fibers capable of demonstrating excellent water rejection, enhanced CO_2 capture capacity, and fast absorption kinetics. While there are examples in the literature[63–70] of electrospun fibers for CO_2 capture, including some using amine-based sorbents as the capture agent, our unique incorporation of hydrophobic ceramic materials for enhanced water rejection addresses both of these issues simultaneously via encapsulation of an effective amine-based sorbent material within highly hydrophobic electrospun polymer-ceramic hybrid fibers.

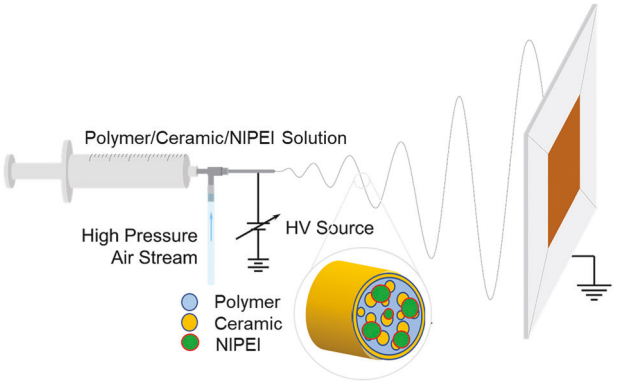

Figure 1. Cartoon schematic depicting the gas-assisted electrospinning setup used in this work featuring an aluminum foil-covered copper collector plate, high voltage source, pressurized air stream, and syringe pump (not shown). A cross-section of the polymer/ceramic/NIPEI fiber is provided for clarity, emphasizing the ceramic shell and internally dispersed NIPEI microdomains.

2. Results and Discussion

To form the electrospun non-woven mats, we first chose to blend PAN with an equal weight of NIPEI to allow for direct comparison with previously published NIPEI-based DAC assemblies.[57,71] To assess the performance of PAN as an encapsulation material for NIPEI, PAN/NIPEI hybrid fibers were electrospun first. Despite the high viscosity of the pure liquid-like NIPEI (>10 000 cP),[47] we observed a negligible viscosity increase after NIPEI was added to the PAN/dimethylformamide (DMF) mixtures. Imaging via optical and scanning electron microscopy (SEM) revealed a fiber diameter of 200 nm to 1 µm for these hybrid fibers. In this work, we employed sessile drop contact angle measurements as a proxy measurement for the bulk-material water rejection potential.

Upon addition of an equal solid-phase loading of NIPEI (50:50 wt.% of PAN:NIPEI), we observed that the highly hydrophobic 140.0 ± 5.9° contact angle associated with pure PAN (**Figure 2**) immediately vanished, and PAN/NIPEI fibers absorbed the incident water droplet. This suggested that some significant fraction of the NIPEI remained at the surface of the fiber. Indeed, examination of the PAN/NIPEI fibers with phase-mapping AC tapping-mode atomic force microscopy (AFM) showed isolated NIPEI domains on the surface (Figure S4, Supporting Information), which could interact with the water droplet. To remedy this, we leveraged previous work by our group in creating polymer-ceramic hybrid materials by blending a low molecular weight liquid-phase slow-curing functionalized organopolysilazane (OPSZ) ceramic precursor with the solution before electrospinning.[72,73] During the spinning process, OPSZ migrated to the outer surface of the polymer jet because of its lower viscosity and surface tension. Subsequent reaction with atmospheric water and oxygen cured and crosslinked the OPSZ into a hydrophobic silica-based ceramic to form a pseudo-coaxial fiber morphology.[72] Three different ceramic precursors (structures provided in Figure S11, Supporting Information) were tested to examine their effects on fiber hydrophobicity: a slow-curing OPSZ, a rapid-curing OPSZ, and a solid-phase

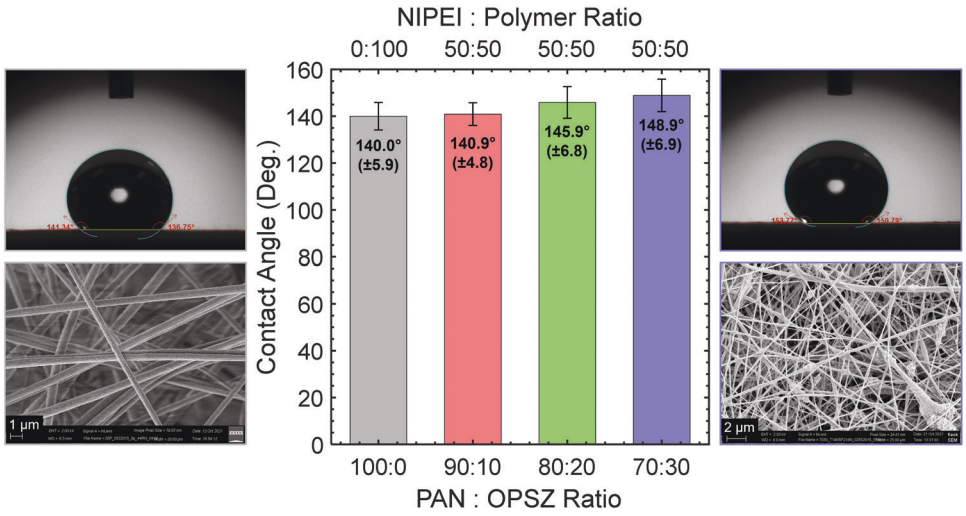

Figure 2. Contact angles observed for PAN fibers (gray) versus 50:50 of NIPEI:(PAN + OPSZ) (red, blue, green) hybrid fibers showing a slight increase in contact angle to nearly-superhydrophobic with at a 70:30 PAN:OPSZ ratio, even with the inclusion of hydrophilic NIPEI. Characteristic contact angle droplets and SEM images are shown for pure PAN (The blue and grey borders are very hard to see left, gray border) and (PAN + OPSZ)/NIPEI (70:30 PAN:OPSZ, right, blue border).

polysilsesquioxane (PSSQ). Only the slow-curing OPSZ yielded hydrophobicity, whereas the rapid-curing OPSZ and PSSQ gave contact angles of 55° and 0°, respectively (Figure S12, Supporting Information). We attributed these results to the formation (or lack thereof) of the ceramic sheath layer on the fiber surface. Both OPSZ materials migrated and cured into a ceramic shell, whereas PSSQ was already a solid upon dissolution into the polymer solution. Therefore, there was no surface tension driving the PSSQ to the surface of the fiber – without sheath layer formation, there was nothing to block the interaction between the dispersed NIPEI and the incident water droplet. Comparing the slow- versus rapid-curing OPSZs, we hypothesized that the lower density of crosslinking groups in the rapid-curing OPSZ was preventing the formation of an adequate hydrophobic layer. Thus, in this manuscript, all future mentions of OPSZ are references to the slow-curing material. It is particularly noteworthy here to emphasize that the OPSZ curing process into its final ceramic state occurs at room temperature, eliminating the need for any heat treatment. Furthermore, the high surface area to volume ratio due to the micron-scale diameter of the fibers, coupled with the shallow thickness of the OPSZ shell, drastically speeds up the curing process to achieve nearly complete curing on the electrospinning timescale.

We found that for the optimized PAN/NIPEI spinning conditions, as little as 10% OPSZ (relative to the quantity of PAN) was necessary to restore the hydrophobicity of the fibers back to ≈140° (140.9 ± 4.8°). Observation of the surface via AFM phase mapping confirmed a smooth, uniform surface (Figures S5, S6, Supporting Information). With the addition of OPSZ, we could incorporate at least an equal weight percentage of an extremely hydrophilic material (NIPEI) into our fibrous matrix without any loss of water rejection potential. As the OPSZ concentration was increased, we observed a slight but notable increase in the contact angle, up to 149.8 ± 6.9° at 70:30 PAN:OPSZ, barely below the 150° threshold for superhydrophobicity. We tested a 60:40 ratio as well (not shown), but increasing the OPSZ content above 70:30 yielded poor fiber quality. We believe this is because in the 60:40 case, enough OPSZ built up on the fiber surface during the migration process to induce noticeable beading as the OPSZ coalesced into discrete droplets of ≈10 µm. Such beading of the OPSZ would cause an uneven distribution of the ceramic precursor, which can negatively affect hydrophobicity (in areas of relatively depleted OPSZ concentrations) and mass transport (in beads with enriched OPSZ concentration). As such, we examined the fiber morphology and carbon dioxide capture performance of PAN:OPSZ ratios of 90:10 (the minimum needed to maintain hydrophobicity), 80:20, and 70:30, all with 50:50 solid-phase polymer NIPEI:(PAN + OPSZ) loadings.

To visualize the spatial distribution of NIPEI within the fiber matrix, we employed two methods: fluorescent tagging and cross-sectional transmission electron microscopy (TEM). The fluorescence visualization study was carried out by tagging the primary amines in the NIPEI corona with a low-concentration solution of fluorescein 5-isothiocyanate (FITC), a common biological tag for visualizing peptides[74–76] (see Supporting Information for experimental details). The tagged NIPEI particles were subsequently encapsulated in the PAN/OPSZ matrix and electrospun, producing bright orange fibers. Imaging via fluorescent confocal microscopy at 488 nm showed excitation of the tagged NIPEI inside the fibers (Figure S2, Supporting Information). We noticed slightly agglomerated areas of greater fluorescence intensity, with the brightest excitation emanating from the fiber beads, indicating that the NIPEI incorporation was not entirely uniform.

To observe the NIPEI distribution in higher resolution, samples of electrospun fibers were embedded in epoxy resin (Embed 812) and microtomed to 70–100 nm both axially and equatorially for TEM imaging. All samples were negatively stained using a 1.5% aqueous solution of uranyl acetate, which is well-known to selectively stain amines and other nucleophilic groups and is particularly prevalent in the imaging of biological materials.[77–79] This stain provides contrast because it selectively complexes with the primary amine functional groups

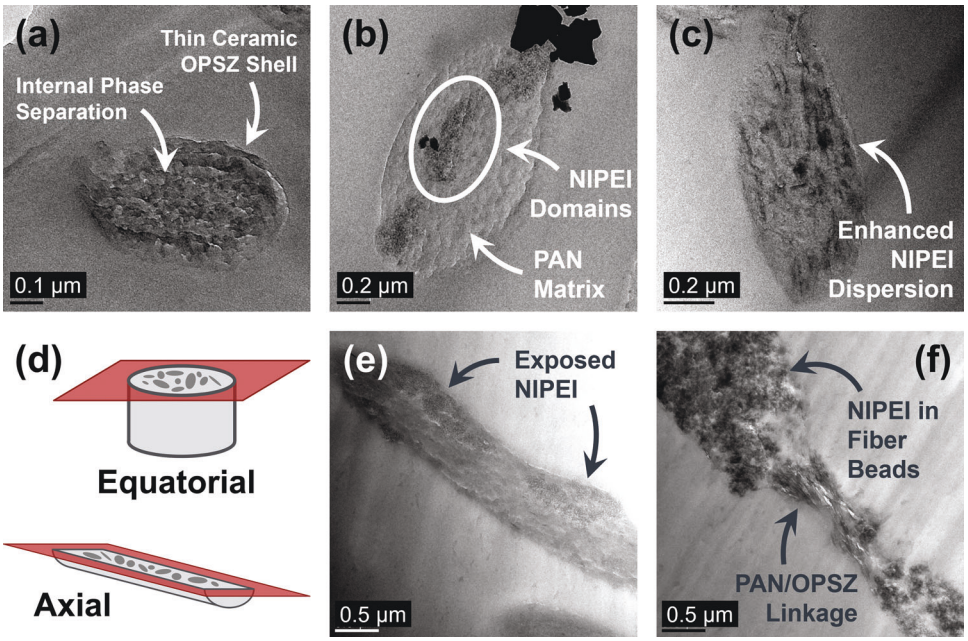

Figure 3. Cross-sectional TEM micrographs of equatorially- a–c) and axially-microtomed e,f) electrospun fibers. a) PAN:OPSZ = 70:30, b,e) PAN:NIPEI = 50:50, c,f) NIPEI:(PAN + OPSZ) = 50:50, PAN:OPSZ = 70:30, d) cartoon of equatorial versus axial fiber planes. All samples were negatively stained with 1.5% uranyl acetate solution for enhanced contrast. Enhanced NIPEI distribution is apparent upon the addition of the OPSZ ceramic precursor.

in the PEI corona of the NIPEI. **Figure 3** shows adjacent TEM images of PAN/OPSZ fibers (Figure 3a), PAN/NIPEI fibers (Figure 3b,e), and (PAN + OPSZ)/NIPEI fibers (Figure 3c,f). In the polymer-ceramic fibers without the inclusion of NIPEI, we saw distinct phase separation between the OPSZ ceramic and the PAN encapsulation polymer, further confirmed by EDX mapping (Figure S7, Supporting Information) showing the uniform presence of silicon within the cross-section. Along the circumference of the fibers containing OPSZ (Figure 3a,c,f) a very thin few-nanometer-thick sheath layer of cured OPSZ ceramic was present around the edge of the fibers, consistent with previously-reported work on polymer-ceramic hybrid fibers.[72] Within PAN/NIPEI fibers without the inclusion of OPSZ (Figure 3b,e), we saw large isolated clusters of negatively stained NIPEI non-uniformly dispersed in the fiber matrix. Solution-phase mixing was able to disperse the bulk NIPEI down to sub-micron-scale domains but was unable to achieve the uniform distribution desired to maximize the effectiveness of each NIPEI particle. After OPSZ was added (70:30 PAN:OPSZ ratio) to the PAN/NIPEI fibers, however, the distribution of stained NIPEI appeared to be considerably more uniform throughout the fiber cross-section in both the equatorial and axial slices (Figure 3c,f). Given that the uncured OPSZ and PEI corona are both comprised of amine chains (functionalized -Si-N-Si-N- for OPSZ versus -CH_2-CH_2-NH- for PEI), we hypothesized that the OPSZ acted as a dispersing agent within the DMF solution during the mixing process by interacting with the PEI corona of the nanoparticles. This allowed for a greater degree of dispersion of the NIPEI nanoparticles in the PAN/OPSZ composite matrix. Still, some agglomerated sub-micron-scale domains remained, primarily in the fiber beads, consistent with the images taken with confocal fluorescence microscopy.

To quantify the amount of NIPEI present within the fibers after electrospinning, we performed thermogravimetric analysis (TGA, Figure S14, Supporting Information). As controls, we analyzed samples of pure PEI, along with PAN/OPSZ fibers with no NIPEI present. Upon combustion of the organic material, we found that pure PEI showed a steady decline followed by a steep fall until 360 °C, where the initial mass loss below 100 °C is due to physisorbed water, and the loss between 100 to 270 °C is the onset of decomposition of the PEI,[80] potentially due to loss from volatility, NH_3, and/or strongly bound water. A large step of decomposition of PEI occurs roughly at 230–360 °C. In the PAN/OPSZ fibers, no degradation was observed until a sharp drop from ≈270 °C to 370 °C, which is attributed to the degradation of C–C bonds in PAN. Additionally, a second loss in mass from 370–580 °C was observed due to the OPSZ additive, with mass remaining from silica formation (which can be seen on the TGA pan). However, upon the addition of NIPEI to the fiber, the TGA curve loses 18 wt.% under 100 °C due to water and the electrospinning solvent. More dramatically, there is a sharp decrease in mass from 100–200 °C for the 80:20 and 70:30 PAN:OPSZ + NIPEI, attributed to potential interactions between the blended materials (such as hydrogen bonding) that weaken the bonds within PEI and catalyze its degradation,[81] causing faster oxidative degradation at a lower temperature than for pure PEI. Interestingly, though, is that with a higher PAN:OPSZ ratio, the degradation temperature onset is significantly lower: 160 °C versus 180 °C for the 80:20 versus 70:30 ratios, respectively. Though in this work it is not aim to study the mechanism of decomposition of these fiber blends, we found that we could reliably calculate the PEI content within the fibers, and, given that NIPEI is composed of 83% PEI and 17% SiO_2, we were able to calculate the loadings of NIPEI in the fibers to be 57.68% (90:10 PAN:OPSZ), 59.77%

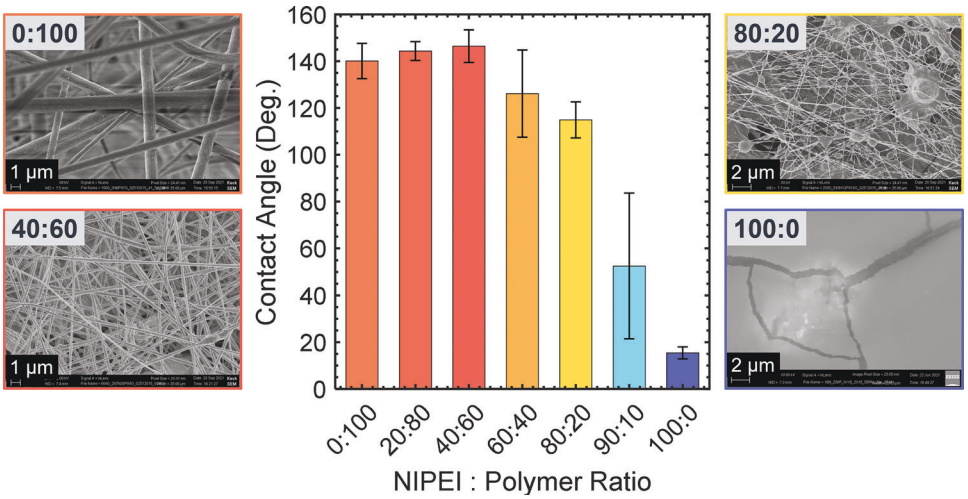

Figure 4. Contact angles for fixed 90:10 PAN:OPSZ ratio and fixed 9.75 wt.% solid content with the NIPEI loading partitioned between pure NIPEI and pure PAN+OPSZ. Selected SEM images are shown for four given NIPEI:(PAN + OPSZ) ratios, highlighting pure PAN/OPSZ (0:100), pure NIPEI (100:0), the maximum contact angle (40:60), and the maximum NIPEI loading while maintaining hydrophobicity (80:20). SEM images for all NIPEI:(PAN + OPSZ) ratios tested are available in Figure S8 (Supporting Information).

(80:20 PAN:OPSZ), and 61.70% (70:30 PAN:OPSZ). These values were notably higher than the 50% solid-phase ratio loaded into the fiber precursor solution, indicating enrichment of the NIPEI content during electrospinning to achieve almost 1.5:1 NIPEI:(PAN + OPSZ) ratios in our fibers, despite the precursor solutions loaded at a 1:1 ratio. Although all the mass left at the end of the TGA experiment is SiO_2, we were unable to deconvolute the contributions from OPSZ and NIPEI and instead opted to use the PEI degradation as a more reliable metric to quantify the NIPEI loading.

Given the effectiveness of the PAN/OPSZ framework toward containing the hydrophilic NIPEI, we sought to determine the maximum loading of NIPEI possible within this matrix before enough NIPEI would necessarily be present on the surface to destroy the hydrophobicity. To this end, we fixed the total solids concentration (PAN + OPSZ + NIPEI) at 9.75% and the PAN:OPSZ ratio at 90:10 based on our preliminary optimizations. The partition between PAN/OPSZ and NIPEI was then modulated from 100% PAN/OPSZ : 0% NIPEI to 0% PAN/OPSZ: 100% NIPEI such that the PAN/OPSZ content would slowly be displaced by the NIPEI, decreasing the percentage of PAN in solution and degrading the fiber quality. In this study, we chose not to simply fix the PAN concentration and increase the NIPEI loading. While this strategy would work for loadings slightly above 1:1 NIPEI:(PAN + OPSZ), we found that high relative loadings of NIPEI quickly caused the solution to become too viscous for reliable fiber formation given the high viscosity of bulk NIPEI. Hence, to ensure we could reliably generate all our precursor solutions, we instead opted to fix the total solids concentration and modulate the partition of PAN/OPSZ and NIPEI. Additionally, we chose to fix the PAN:OPSZ ratio at 90:10 for all solutions to minimize the addition of components of the system, as only a 90:10 ratio is required to maintain hydrophobicity.

After electrospinning fiber mats for each NIPEI:(PAN + OPSZ) ratio, the resultant morphologies and corresponding hydrophobicities were characterized by SEM and contact angle measurements, respectively. We found the average contact angle remained above 140° until a 2:3 ratio of NIPEI:(PAN + OPSZ), after which the contact angle plateaus ≈115–120°. Increasing the relative loading past a 4:1 ratio of NIPEI:(PAN + OPSZ), we observed a precipitous drop, eventually settling at the 15.4 ± 2.6° angle of pure NIPEI (**Figure 4**). The quality of electrospun fibers was highly dependent on the concentration of PAN in the solution, so the fiber diameter and uniformity deteriorated with decreasing PANg/OPSZ percentage. As the relative amount of NIPEI increased, the decreased percentage of PAN in solution resulted in the electrospun fiber diameter decreasing by nearly two orders of magnitude, from ≈1 μm (pure PAN/OPSZ fibers) to only tens of nanometers (80% NIPEI: 20% (PAN + OPSZ)) (Figure S8, Supporting Information). At the threshold of 80% NIPEI (1.77 wt.% PAN in solution, down from 7.5% with PAN/OPSZ only), we observed the fibers to be heavily beaded and interrupted by spherical nodules of the (PAN + OPSZ)/NIPEI bulk material. We interpreted this 80% loading to be the threshold at which point the volume to the surface area was no longer high enough to encapsulate the added NIPEI. This threshold was, however, considerably higher than expected, indicating that we could incorporate as much as 4 times more NIPEI than the matrix and encapsulation material without loss of hydrophobicity.

To understand the CO_2 capture performance and capabilities of this system, control samples of electrospun fibers containing only polymer and ceramic in the 90:10, 80:20, and 70:30 PAN:OPSZ ratios were degassed and pre-treated with N_2 at 120 °C, then exposed to 99.9+% CO_2 for five hours at 30 °C. In each case, a nearly negligible quantity of CO_2 was absorbed per gram of sorbent material (**Figure 5**a). Given the absence of NIPEI and the lack of nucleophilic functional groups in the PAN and cured OPSZ ceramic, the encapsulation matrix itself naturally exhibited a very low affinity toward carbon dioxide. Fibers featuring 50–60% loadings of NIPEI by weight and the same PAN/OPSZ ratios were then tested. Once NIPEI was introduced, we observed

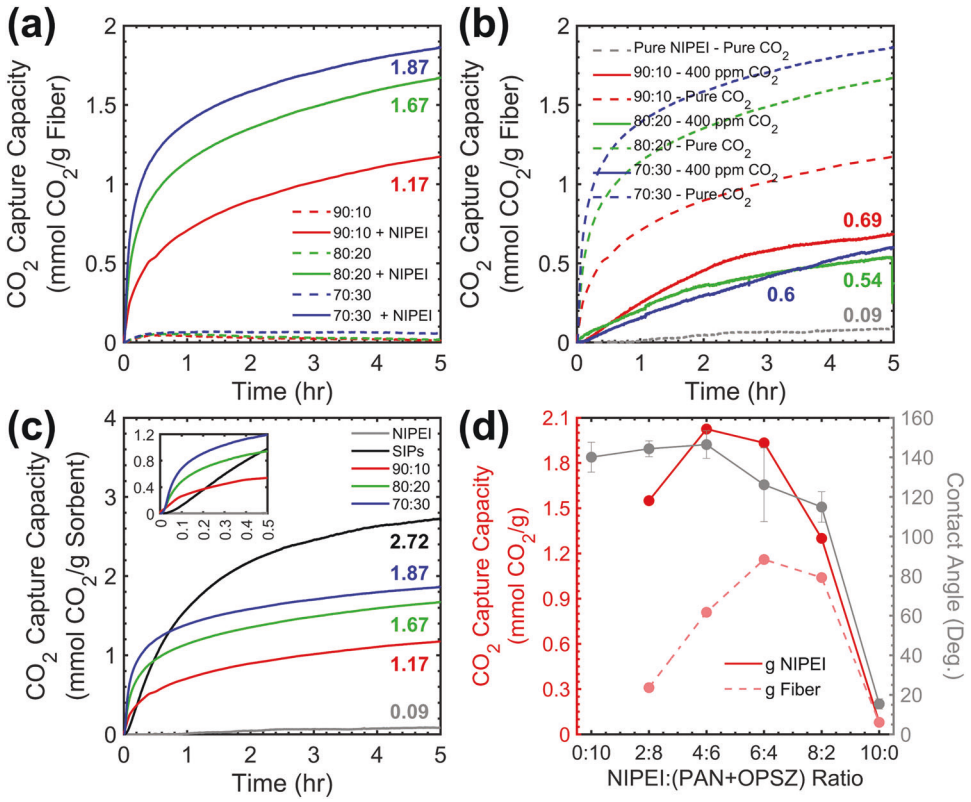

Figure 5. CO_2 capture capacities for a) PAN/OPSZ fibers with and without incorporation of NIPEI in bone-dry pure CO_2 (P_{CO2} = 1 atm), normalized by NIPEI loading, emphasizing the requirement of NIPEI for CO_2 uptake, b) (PAN + OPSZ)/NIPEI fibers capture capacities in pure (dashed lines) versus 400 ppm CO_2 (solid lines) per gram fiber, c) comparison of (PAN + OPSZ)/NIPEI fibers with pure NIPEI and with SIPs (TEGO Rad 2650 polymer matrix, 49 wt.% loading)[57] in pure CO_2, and d) (PAN + OPSZ)/NIPEI fibers with fixed solid content and NIPEI:(PAN + OPSZ) loading ramped from 0:100 (pure PAN + OPSZ) to 100:0 (pure NIPEI) at 400 ppm CO_2 plotted alongside measured contact angles.

the CO_2 uptake to increase dramatically to 1.17 mmol CO_2 g^{-1} fiber in the case of 90:10 PAN:OPSZ and 1.67 and 1.87 mmol CO_2 g^{-1} fiber in the 80:20 and 70:30 samples, respectively. A schematic for CO_2 capture via carbamate formation is given in Figure S16 (Supporting Information). Interestingly, we observed an increase in the CO_2 uptake with an increasing proportion of OPSZ, despite the prior evidence that OPSZ is not participating in the capture capacity. We hypothesized that this resulted from two factors: the improved dispersion of NIPEI upon the addition of OPSZ (Figure 3c,f) and the PAN/OPSZ phase separation creating enlarged internal surface area through increased tortuosity (Figure S7a, Supporting Information).

Upon exposure of the same (PAN + OPSZ)/NIPEI fibers to DAC conditions of 400 ppm dry CO_2, balance N_2 (Figure 5b), we observed a noticeable decrease in the kinetics of the CO_2 uptake, with the 90:10 and 80:20 PAN:OPSZ ratios barely reaching saturation after 5 h, and the 70:30 PAN:OPSZ fibers having yet to reach full capacity. We attributed this to the considerably diminished CO_2 concentration gradient between the working gas and the sample. More interestingly, however, the pure CO_2 trend showing increased capacity with increased OPSZ addition seemed to be reversed in the 400 ppm trials. Now, 90:10 PAN:OPSZ gave the highest capacity at 0.69 mmol CO_2 g^{-1} fiber, with 80:20 and 70:30 showing comparable 0.54 mmol CO_2 g^{-1} fiber and 0.60 mmol CO_2 g^{-1} fiber, respectively. Looking at the shape of these uptake curves, the 90:10 trace showed the highest curvature and the 70:30 the lowest (i.e., the most linear). Since the CO_2 must pass through the ceramic shell to interact with the NIPEI, we hypothesized that under 400 ppm conditions, the thickness of this shell now played a crucial role in the transport of CO_2 into the fiber interior. Previous studies[72] of PAN/OPSZ fibers showed that in the 90:10 ratio, this ceramic shell was ≈3 nm in thickness but was increased to ≈6 nm in the 70:30 ratio. Because the concentration gradient of CO_2 was now no longer sufficient to overcome this transport resistance, the effect of only a few nanometers became noticeably present, with transport into the fiber much faster at low OPSZ loadings. Thus, while high OPSZ ratios were ideal for a CO_2-rich gas stream, under atmospheric concentrations, low OPSZ loadings were crucial to achieving good kinetic performance over multiple adsorption/desorption cycles. Although the kinetics of the uptake changed significantly when the CO_2 in the process gas was decreased, we observed that the total capture capacities maintained the same order of magnitude. Despite the reduction in the partial pressure of CO_2 by a factor of 2500 (1 atm to 0.0004 atm), the measured capacity only dropped by a factor of between 1.5 and 3, indicating consistent performance under a more realistic DAC environment.

The electrospun fibers developed in this work also exhibited enhanced CO_2 capture kinetics when compared with similar encapsulated NIPEI systems previously reported. For example, the

fibers demonstrated faster initial CO_2 capture than Solvent Impregnated Polymers (SIPs), which have a similar membrane-like geometry that is composed of encapsulated solvent microdroplets within a CO_2-permeable crosslinked polymer network.[71] While SIPs can support higher NIPEI loadings and therefore yield higher total capacities,[4] our fibers exhibited more rapid CO_2 uptake due to the nonwoven morphology (Figure 5c,c inset), which reduces the pressure drop and increases the surface area available to bulk airflow via the through-pores of the nonwoven mat (size distributions shown in Figures S9–S11, Supporting Information). Additionally, micron-scale fiber diameters that enable microdispersions of NIPEI collectively reduce the distance required for the CO_2 to diffuse through the OPSZ sheath layer into the PAN/OPSZ matrix to interact with the embedded NIPEI.

Finally, samples of the fibers containing a fixed 90:10 PAN:OPSZ composition (since this was the minimum OPSZ concentration required to achieve hydrophobicity) and modulated NIPEI:(PAN + OPSZ) ratios (contact angles shown in Figure 4) were tested for their CO_2 capture capabilities in 400 ppm CO_2 and ambient temperatures. We observed that the capture capacity increased with increasing NIPEI incorporation at a constant PAN:OPSZ ratio, peaking at a NIPEI:(PAN + OPSZ) ratio of 6:4 with a capacity of 1.16 mmol CO_2 g^{-1} fiber, then decreasing back down slightly to 1.04 mmol CO_2 g^{-1} fiber at 8:2 NIPEI:(PAN + OPSZ) before reaching effectively negligible capacity in the absence of a supporting fibrous matrix. When we normalized these capacities per gram of encapsulated NIPEI, we found the maximum to shift toward lower NIPEI loadings, with the peak now at 4:6 NIPEI:(PAN + OPSZ) (0.83 mmol CO_2 g^{-1} fiber or 2.03 mmol CO_2 g^{-1} NIPEI), very closely followed by the 6:4 ratio (1.16 mmol CO_2 g^{-1} fiber or 1.93 mmol CO_2 g^{-1} NIPEI), indicating the 4:6 ratio was slightly more efficient with the encapsulated amine. Given that a pure NIPEI film was quite poor at capturing CO_2 as discussed previously, it was expected that the CO_2 uptake of these films would not always increase with increasing relative NIPEI loading. Instead, there was an apparent balancing act between two competing factors. Enough NIPEI must have been present in the fiber matrix to make full use of the advantages of fibrous encapsulation. However, adding too much NIPEI caused the concentration of PAN in the solution to drop to a percentage below which reliable fibers failed to form, and there was not enough encapsulation medium to contain and disperse the high loadings of NIPEI, which is the same factor resulting in the sharp drop in contact angle above 80% relative NIPEI in Figure 4. The peak at 6:4 NIPEI:(PAN + OPSZ) (per g fiber) was slightly lower than our bulk contact angle measurements, where we saw a loss of hydrophobicity at higher loadings than the 8:2 ratio (114.9 ± 7.7°). By crossing this threshold, some NIPEI was inherently on the surface of the thin fibers once the diameters were on the order of tens of nanometers. However, we have demonstrated optimization of our CO_2 capture by incorporating four times greater loading of NIPEI with respect to encapsulation polymer.

3. Conclusion

Diffusion limitations through bulk NIPEI, formation of a passivating carbamate skin layer, and high affinity for water prevent neat NIPEI from reaching its full potential as a carbon capture agent. We sought to remedy these drawbacks by dispersing NIPEI via encapsulation within submicron-scale polyacrylonitrile(PAN)/polymer-derived-ceramic electrospun fibers. The addition of a room-temperature curable, liquid-phase organopolysilazane (OPSZ) ceramic precursor to the PAN/NIPEI solution enhanced the internal dispersion of NIPEI, producing a near-uniform distribution throughout the fiber cross-section. The low surface tension and viscosity of OPSZ facilitated its migration to the fiber surface during electrospinning, forming a few-nanometer-thick exterior shell. Upon curing into a hydrophobic ceramic, this layer shielded the NIPEI from external water to produce near-superhydrophobic non-woven fiber mats with contact angles exceeding 140°. 1:1–1.5:1 loadings of NIPEI:(PAN + OPSZ) can be reliably achieved with low OPSZ loadings, and up to 4:1 NIPEI:(PAN + OPSZ) loadings are possible before loss of hydrophobicity. These fibers demonstrated high capture capacities of up to 1.87 mmol CO_2 g^{-1} fiber in a pure CO_2 atmosphere with excellent kinetics due to enhanced surface interactions within the non-woven fiber network to overcome diffusion limitations. The fibers additionally showed excellent performance retention under 400 ppm CO_2 direct air capture conditions with only a 1.5–3x drop in capture capacity, highlighting the selectivity of the system toward CO_2 over other gases. Ramping the NIPEI concentration from 0 to 100% showed peak CO_2 capacity at a 4:6 ratio of NIPEI:(PAN + OPSZ) (0.83 mmol CO_2 g^{-1} fiber = 2.03 mmol CO_2 g^{-1} NIPEI), with capacity above 1 mmol CO_2 g^{-1} fiber extending to the hydrophobicity edge of 8:2 NIPEI:(PAN + OPSZ). Future work on these fibers is focused on examining their cycling stability and performance in 400 ppm CO_2 environments under variable temperatures and humidity levels to understand their applicability to global DAC installations.

4. Experimental Section

Materials: Polyacrylonitrile (PAN, M_w = 200 kDa, Polysciences, Inc.) was purchased as a fine powder and used without further purification. Dimethylformamide (Sigma Aldrich) was used as received in the electrospinning process without further drying. NOHM-I-PEI was prepared as in ref. [57]. The NIPEI was dried under vacuum at 80 °C for three hours prior to use in electrospun hybrid fibers to remove residual water from the synthesis process. Durazane 1500 Slow Cure and Durazane 1500 Rapid Cure organopolysilazane (OPSZ) liquid ceramic precursors were purchased from durXtreme GmbH and stored at room temperature. Acrylate-terminated ladder-structure polysilsesquioxane (PSSQ) was received from DJ Semichem. FITC was purchased from Sigma Aldrich, stored at 0 °C, and used as received. Pure CO_2, argon and 400 ppm CO_2 in N_2 were purchased from Airgas.

Preparation of Polymer Solutions: Solid precursors NIPEI and PAN were loaded into a 20 mL scintillation vial, followed by liquid organopolysilazane. DMF was added, and the solution was left to stir at room temperature until homogenization was observed, at a minimum overnight. All concentrations in this manuscript were reported as the weight of the component per total weight of the solution. As an example, a PAN/OPSZ/NIPEI solution with 70:30 PAN:OPSZ ratio and 50% relative NIPEI loading with 7 wt.% PAN will contain 7 wt.% PAN, 3 wt.% OPSZ (70:30 concentration ratio), and 10 wt.% NIPEI (50% of total dissolved solids are NIPEI). The remaining 80 wt.% (i.e., 100% − 7% − 3% − 10%) of the solution was composed of the DMF solvent.

Electrospinning: Polymer solutions were loaded into a plastic syringe (BD Plastic-Pak, 5 mL) fitted with a custom three-way Luer-Lock fitting with an inner 16-gauge extrusion needle. The syringe was placed into a syringe pump (Ph.D. Ultra, Harvard Apparatus) 15 cm from a stationary grounded copper collector plate covered in aluminum foil. A voltage of 20 kV was applied between the needle and the grounding plate, and the polymer solution was extruded at a fixed flow rate of 0.025 mL min^{-1} (1.5 mL hr^{-1}). For polymer fibers spun at low PAN concentrations that proved too fragile to spin directly onto aluminum, a layer of coarse polyethylene terephthalate (PET) filter media (SNT Inc., Korea, 30 g m^{-2} areal mass) was attached to the aluminum foil with conductive carbon tape, and the fibers were deposited onto this PET backing. Relative humidity was controlled via a small humidifier placed inside the enclosure. The humidifier was allowed to run until the relative humidity in the chamber reached the upper bound of the desirable window (25–35%), then the electrospinning was performed. It was found that the quality of the fibers was not heavily dependent on flow rate, voltage bias, or collector distance, and single- or few-micron morphologies could be maintained with some variability of these factors (e.g., ±0.025 mL min^{-1}, ±5 kV, and ±2.5–5 cm). However, the morphology was very susceptible to the relative humidity. At relative humidities greater than 30–35%, the diameters were very inconsistent, the fiber mat had trouble adhering to the collector plate, and the surface of the mat was highly uneven.

Microscopy Characterization: Electrospun fibers were initially characterized via optical microscopy (AmScope) Sections of the fiber mat were removed with tweezers, mounted onto a glass slide, and covered with a plastic cover slip. Sections of the electrospun fiber mat still on the aluminum foil collector material were cut out and mounted on aluminum stubs with conductive carbon tape. All samples were sputter coated with a thin layer of Au/Pd alloy to enhance conductivity and mitigate charging. Images were taken using either an LEO 1550 FESEM or Zeiss Gemini 500 SEM using a 2 kV extraction voltage. Fiber samples were first embedded in epoxy resin (Embed 812) and cured at 80 °C for a minimum of 12 h. Embedded samples were microtomed to 70–100 nm (Leica Ultracut UCT Ultramicrotome). Negative staining with uranyl acetate (UA) was carried out with a 1.5% aqueous solution of UA. Microtomed samples were exposed for 15 min, then washed three times with distilled water before drying and imaging. Bright-field transmission electron microscopy images were taken on an FEI F20 TEM STEM at 200 kV extraction voltage using a 50 µm aperture, spot size 3. Caution: Uranium (natural isotope ^{238}U) is an α-emitter with a half-life of 4.463×10^9 years and a decay energy of 4.187 MeV.[82] Manipulations were performed in a fume hood equipped with appropriate radioactivity-sensing equipment. AFM samples were prepared by spinning a thin layer of the fibrous material onto aluminum foil attached to a glass microscope slide by conductive carbon tape. Images were taken on an Asylum MFP-3D instrument using AC air topography operated in tapping mode at ~5% of the cantilevered resonance frequency. The acquisition was performed with a scanning rate of 0.2–0.5 µm s^{-1} and a resolution of 256 points and lines. A sample of fluorescent-tagged fibers was loaded onto a glass microscope slide, wetted with silicon oil (Sigma Aldrich), and covered with a #1.5 glass cover slip. The slide was placed on the stage of a 3i Marianas confocal microscope and excited with a laser wavelength of 488 nm. Z-stack images were collected within Slidebook software.

Contact Angle: The hydrophobicity of the fiber mats was probed via sessile drop contact angle measurements (Theta Lite Optical Tensiometer, Biolin Scientific) using DI water as the liquid phase. A sample of the fiber mat with foil backing was attached to a plastic coverslip with double-sided tape, and a droplet of water (≈10 µL) was deposited via a gas-tight syringe fitted with a Vernier plunger. For hydrophobic samples, contact angles were taken for a minimum of 60 s to ensure the stability of the angle, for hydrophilic samples, 180 to 300 s recording times were used to reach the steady value. Angles on the left and right sides of the water droplet were collected and averaged to give the value for each trial. Five to six contact measurements were recorded and averaged for each fiber mat to give the final reported value.

Thermogravimetric Analysis (TGA): Both a Discovery 5500 TA Instruments TGA and a LABSYS evo, Setaram was used for gravimetric pseudo-equilibrium carbon adsorption capacity measurements and thermal decomposition. Thermal decomposition was conducted under air at 10 °C per minute up to 600 and 700 °C products of decomposition were analyzed by an in-line Cirrus 3 Mass Spectrometer. Pseudo-equilibrium capacities were conducted at 30 °C using a mixture of 400 ppm CO_2 balanced with nitrogen or 99.9+% CO_2. Samples were first dried and pre-treated in the TGA under a flow of argon at 90 °C at a ramp rate of 10 °C min^{-1} and held for 2 h. The temperature was rapidly cooled to 30 °C and equilibrated for 30 min, followed by switching the gas flow to the 400 ppm CO_2/N_2 mix or CO_2 and held for up to 6 h. Regeneration was conducted between each adsorption cycle, with initial conditions of 90 °C for 2 h in argon and repeating the cycles.

Capillary Flow Porometry: Through-pores were measured via capillary flow porometry (CFP-1100-AEHXL, Porous Materials Inc.). Circular samples measuring one inch in diameter were cut from the electrospun fibrous mat, peeled from the aluminum foil backing, and loaded into the instrument. A dry run with increasing incident airflow was first performed with no wetting liquid, then the sample was saturated with silicone oil (SilWick, surface tension = 20.1 dyne cm^{-1}) before the following wet run was performed under identical conditions.

Supporting Information

Supporting Information is available from the Wiley Online Library or from the author.

Acknowledgements

K.D.K. performed all electrospinning work and microscopy, porometry, and contact angle characterization for the polymer fibers in this study. CO_2 capture tests were performed by G.H.L., J.H.X., and M.K.K. TGA analysis to determine the NIPEI loadings was performed by M.K.K. and G.H.L. NIPEI was synthesized by G.H.L. The manuscript was written by K.D.K., with the CO_2 capture methods and TGA methods sections provided by G.H.L. and M.K.K. Conceptualization and project supervision at Cornell was done by Y.L.J., while project supervision at ORNL and Columbia was carried out by M.K.K and A.-H.A.P., respectively. The authors acknowledge the funding for this work provided by the Office of Fossil Energy Carbon Managment in the U.S. Department of Energy (DE-FE0031963 and FWP 3FEAA392). This work also made use of the Cornell Center for Materials Research Shared Facilities, which were supported through the NSF MRSEC program (DMR-1719875). Notice: This manuscript was authored by UT-Battelle, LLC, under contract DE-AC05-00OR22725 with the US Department of Energy (DOE). The US government retains and the publisher, by accepting the article for publication, acknowledges that the US government retains a nonexclusive, paid-up, irrevocable, worldwide license to publish or reproduce the published form of this manuscript or allow others to do so, for US government purposes. DOE will provide public access to these results of federally sponsored research in accordance with the DOE Public Access Plan (http://energy.gov/downloads/doe-public-access-plan).

Conflict of Interest

The authors declare no conflict of interest.

Data Availability Statement

The data that support the findings of this study are available from the corresponding author upon reasonable request.

Keywords

CO_2 capture, direct air capture, gas-assisted electrospinning, nanoparticle organic hybrid materials, polymer-ceramic hybrid fibers, selective water rejection

Received: February 12, 2023
Revised: April 2, 2023
Published online: May 16, 2023

[1] IPCC, 2022:Climate Change 2022: *Mitigation of Climate Change. Contribution of Working Group III to the Sixth Assessment Report of the Intergovernmental Panel on Climate Change*, (Eds.: P. R. Shukla, J. Skea, R. Slade, A. Al Khourdajie, R. van Diemen, D. McCollum, M. Pathak, S. Some, P. Vyas, R. Fradera, M. Belkacemi, A. Hasija, G. Lisboa, S. Luz, J. Malley), Cambridge University Press, Cambridge, UK and New York, NY, USA, https://doi.org/10.1017/9781009157926.
[2] A. Samanta, A. Zhao, G. K. H. Shimizu, P. Sarkar, R. Gupta, *Ind. Eng. Chem. Res.* **2011**, *51*, 1438.
[3] J. C. Hicks, J. H. Drese, D. J. Fauth, M. L. Gray, G. Qi, C. R. Jones, *J. Am. Chem. Soc.* **2008**, *130*, 2902.
[4] G. D. Pirngruber, S. Cassiano-Gaspar, S. Louret, A. Chaumonnot, B. Delfort, *Energy Procedia* **2009**, *1*, 1335.
[5] X. Xu, C. Song, B. G. Miller, A. W. Scaroni, *Fuel Process. Technol.* **2005**, *86*, 1457.
[6] S. Choi, J. H. Drese, C. W. Jones, *ChemSusChem* **2009**, *2*, 796.
[7] G. Li, P. Xiao, P. Webley, J. Zhang, R. Singh, M. Marshall, *Adsorption* **2008**, *14*, 415.
[8] F. Su, C. Lu, W. Cnen, H. Bai, J. F. Hwang, *Sci. Total Environ.* **2009**, *407*, 3017.
[9] M. Radosz, X. Hu, K. Krutkramelis, Y. Shen, *Ind. Eng. Chem. Res.* **2008**, *47*, 3783.
[10] P. Davini, *Carbon* **2002**, *40*, 1973.
[11] A. B. Rao, E. S. Rubin, *Environ. Sci. Technol.* **2002**, *36*, 4467.
[12] A. Sayari, Y. Belmabkhout, R. Serna-Guerrero, *Chem. Eng. J.* **2011**, *171*, 760.
[13] A. Ö. Yazadin, R. Q. Snurr, T.-H. Park, K. Koh, J. Liu, M. D. LeVan, A. I. Benin, P. Jakubczak, M. Lanuza, D. B. Galloway, J. J. Low, R. R. Willis, *J. Am. Chem. Soc.* **2009**, *131*, 18198.
[14] Y. C. Park, S.-H. Jo, C. K. Ryu, C.-K. Yi, *Energy Procedia* **2009**, *1*, 1235.
[15] J. B. Lee, C. K. Ryu, J.-I. Baek, J. H. Lee, T. H. Eom, S. H. Kim, *Ind. Eng. Chem. Res.* **2008**, *47*, 4465.
[16] H. Hayashi, J. Taniuchi, N. Furuyashiki, S. Sugiyama, S. Hirano, N. Shigemoto, T. Nonaka, *Ind. Eng. Chem. Res.* **1998**, *37*, 185.
[17] V. G. Gomes, K. W. K. Yee, *Sep. Purif. Technol.* **2002**, *28*, 161.
[18] Y. Takamura, S. Narita, J. Aoki, S. Hironaka, S. Uchida, *Sep. Purif. Technol.* **2001**, *24*, 519.
[19] B.-K. Na, K.-K. Koo, H.-E. Eun, H. Lee, H. K. Song, *Korean J. Chem. Eng.* **2001**, *18*, 220.
[20] E. S. Kikknides, R. T. Yang, *Ind. Eng. Chem. Res.* **1993**, *32*, 2714.
[21] X. Zhao, Q. Cui, B. Wang, X. Yan, S. Singh, F. Zhang, X. Gao, Y. Li, *Chin. J. Chem. Eng.* **2018**, *26*, 2292.
[22] A. Schäffer, K. Brechtel, G. Scheffknecht, *Fuel* **2012**, *101*, 148.
[23] B. Zhu, Q. Liu, Q. Zhou, J. Yang, J. Ding, J. Wen, *Chem. Eng. Technol.* **2014**, *37*, 635.
[24] A. Wilk, L. Więcław-Solny, D. Śpiewak, T. Spietz, H. Kierzkowska-Pawlak, *Chem. Process Eng.* **2015**, *36*, 49.
[25] a) G. T. Rochelle, *Science* **2009**, *325*, 1652; b) B. Dutcher, M. Fan, A. G. Russell, *ACS Appl. Mater. Interfaces* **2015**, *7*, 2137.
[26] L. Dumée, C. Scholes, G. Stevens, S. Kentish, *Int. J. Greenhouse Gas Control* **2012**, *10*, 443.
[27] J. Yu, S. S. C. Chuang, *Ind. Eng. Chem. Res.* **2017**, *56*, 6337.
[28] T. C. Drage, A. Arenillas, K. M. Smith, C. E. Snape, *Microporous Mesoporous Mater.* **2008**, *116*, 504.
[29] S. A. Bedell, *Int. J. Greenhouse Gas Control* **2011**, *5*, 1.
[30] C. Gouedard, D. Picq, F. Launay, P. L. Carrette, *Int. J. Greenhouse Gas Control* **2012**, *10*, 244.
[31] A. Heydari-Gorji, Y. Belmabkhout, A. Sayari, *Microporous Mesoporous Mater.* **2011**, *145*, 146.
[32] B. R. Strazisar, R. R. Anderson, C. M. White, *Energy Fuels* **2003**, *17*, 1034.
[33] H. Lepaumier, D. Picq, P.-L. Carrette, *Ind. Eng. Chem. Res.* **2009**, *48*, 9061.
[34] H. Lepaumier, D. Picq, P.-L. Carrette, *Ind. Eng. Chem. Res.* **2009**, *48*, 9068.
[35] H. Lepaumier, S. Martin, D. Picq, B. Delfort, P.-L. Carrette, *Ind. Eng. Chem. Res.* **2010**, *49*, 4553.
[36] a) S. A. Bedell, *Energy Procedia* **2009**, *1*, 771; b) P. Bollini, S. Choi, J. H. Drese, C. W. Jones, *Energy Fuels* **2011**, *25*, 2416.
[37] A. Sayari, Y. Belmabkhout, *J. Am. Chem. Soc.* **2010**, *132*, 6312.
[38] R. A. Khatri, S. S. C. Chuang, Y. Soong, M. L. Gray, *Energy Fuels* **2006**, *20*, 1514.
[39] J. Davis, G. Rochelle, *Energy Procedia* **2009**, *1*, 327.
[40] K.-Y. Andrew Lin, Y. Park, C. Petit, A.-H. A. Park, *RSC Adv.* **2014**, *4*, 65195.
[41] A. Heydari-Gorji, A. T. Sayari, *Ind. Eng. Chem. Res.* **2012**, *51*, 6887.
[42] R. Rodriguez, R. Herrera, L. A. Archer, E. P. Giannelis, *Adv. Mater.* **2008**, *20*, 4353.
[43] Y. Park, D. Shin, Y. N. Jang, A.-H. A. Park, *J. Chem. Eng. Data* **2011**, *57*, 40.
[44] T. G. Feric, S. T. Hamilton, N. M. Cantillo, A. E. Imel, T. A. Zawodzinski, A. A. Park, *J. Phys. Chem. B* **2021**, *125*, 9223.
[45] P. Nath, R. Mangal, F. Kohle, S. Choudhury, S. Narayanan, U. Wiesner, L. A. Archer, *Langmuir* **2018**, *34*, 241.
[46] Y. Park, C. Petit, P. Han, A.-H. Alissa Park, *RSC Adv.* **2014**, *4*, 8723.
[47] C. Petit, S. Bhatnagar, A. H. Park, *J. Colloid Interface Sci.* **2013**, *407*, 102.
[48] J. Wang, W. Fang, J. Luo, M. Gao, Y. Wan, S. Zhang, X. Zhang, A.-H. A. Park, *J. Membr. Sci.* **2019**, *584*, 79.
[49] D. Wang, S. Song, W. Zhang, Z. He, Y. Wang, Y. Zheng, D. Yao, Y. Pan, Z. Yang, Z. Meng, Y. Li, *Sep. Purif. Technol.* **2020**, *241*, 116708.
[50] K.-Y. A. Lin, H. Yang, W.-D. Lee, K.-Y. Tsao, *J. Mol. Liq.* **2015**, *204*, 50.
[51] A. B. Bourlinos, R. Herrera, N. Chalkias, D. D. Jiang, Q. Zhang, L. A. Archer, E. P. Giannelis, *Adv. Mater.* **2005**, *17*, 234.
[52] A. B. Bourlinos, A. Stassinopoulos, D. Anglos, R. Herrera, S. H. Anastasiadis, D. Petridis, E. P. Giannelis, *Small* **2006**, *2*, 513.
[53] A. B. Bourlinos, S. Ray Chowdhury, R. Herrera, D. D. Jiang, Q. Zhang, L. A. Archer, E. P. Giannelis, *Adv. Funct. Mater.* **2005**, *15*, 1285.
[54] S. C. Warren, M. J. Banholzer, L. S. Slaughter, E. P. Giannelis, F. J. DiSalvo, U. B. Wiesner, *J. Am. Chem. Soc.* **2006**, *128*, 12074.
[55] K. Y. Lin, A. H. Park, *Environ. Sci. Technol.* **2011**, *45*, 6633.
[56] Y. Park, J. Decatur, K. Y. Lin, A. H. Park, *Phys. Chem. Chem. Phys.* **2011**, *13*, 18115.
[57] G. Rim, T. G. Feric, T. Moore, A. H. A. Park, *Adv. Funct. Mater.* **2021**, *31*, 2010047.
[58] Y. Zhmayev, G. L. Shebert, S. Pinge, P. Kaur, H. Liu, Y. L. Joo, *Polymer* **2019**, *178*, 121551.
[59] G. Shoorideh, Y. S. Kim, Y. L. F. Joo, *Electrochim. Acta* **2016**, *222*, 946.
[60] Y. Zhmayev, S. Pinge, G. Shoorideh, G. L. Shebert, P. Kaur, H. Liu, Y. L. Joo, *Small* **2016**, *12*, 5543.
[61] L. Fei, B. P. Williams, S. H. Yoo, J. M. Carlin, Y. L. Joo, *Chem. Commun.* **2016**, *52*, 1501.
[62] L. Fei, B. P. Williams, S. H. Yoo, J. Kim, G. Shoorideh, Y. L. Joo, *ACS Appl. Mater. Interfaces* **2016**, *8*, 5243.
[63] Y.-J. Heo, Y. Zhang, K. Y. Rhee, S.-J. Park, *Composites, Part B* **2019**, *156*, 95.
[64] D. Nan, J. Liu, W. Ma, *Chem. Eng. J.* **2015**, *276*, 44.
[65] D. W. Kim, D. W. Jung, A. A. Adelodun, Y. M. Jo, *J. Appl. Polym. Sci.* **2017**, *134*, 45534.
[66] G. Zainab, A. A. Babar, N. Iqbal, X. Wang, J. Yu, B. Ding, *Compos. Commun.* **2018**, *10*, 45.

[67] J. Wang, A. A. Adelodun, J. M. Oh, Y. M. Jo, *Nano Convergence* **2020**, *7*, 7.
[68] S. H. Pang, M. L. Jue, J. Leisen, C. W. Jones, R. P. Lively, *ACS Macro Lett.* **2015**, *4*, 1415.
[69] C. R. Mason, L. Maynard-Atem, K. W. Heard, B. Satilmis, P. M. Budd, K. Friess, M. Lanc, P. Bernardo, G. Clarizia, J. C. Jansen, *Macromolecules* **2014**, *47*, 1021.
[70] L. Olivieri, M. Roso, M. G. De Angelis, A. Lorenzetti, *J. Membr. Sci.* **2018**, *546*, 128.
[71] T. Moore, M. Biviano, K. A. Mumford, R. R. Dagastine, G. W. Stevens, P. A. Webley, *Ind. Eng. Chem. Res.* **2019**, *58*, 6626.
[72] S. A. Smith, J. H. Park, B. P. Williams, Y. L. Joo, *J. Mater. Sci.* **2016**, *52*, 3657.
[73] S. A. Smith, B. P. Williams, Y. L. Joo, *J. Membr. Sci.* **2017**, *526*, 315.
[74] T. H. The, T. E. W. Feltkamp, *Immunology* **1970**, *18*, 865.
[75] S. S. Twining, *Anal. Biochem.* **1984**, *143*, 30.
[76] K. L. Holmes, L. M. Lantz, in *Cytometry*, Academic Press, Cambridge **2001**, *63*, pp. 185.
[77] M. L. Watson, *J. Biophys. Biochem. Cytol.* **1958**, *4* , 475.
[78] J. C. Tapia, N. Kasthuri, K. J. Hayworth, R. Schalek, J. W. Lichtman, S. J. Smith, J. Buchanan, *Nat. Protoc.* **2012**, *7*, 193.
[79] R. Håkanson, C. Owman, B. Sporrong, F. Sundler, *Histochemie* **1971**, *27*, 226.
[80] Y. Tan, Z.-B. Shao, L.-X. Yu, Y.-J. Xu, W.-H. Rao, L. Chen, Y.-Z. Wang, *Polym. Degrad. Stab.* **2016**, *131*, 62.
[81] M. Vasquez-Rendon, M. Lucia Alvarez-Lainez, *Polymer* **2018**, *154*, 241.
[82] Live Chart of Nuclides. International Atomic Energy Agency – Nuclear Data Section, https://www-nds.iaea.org/relnsd/vcharthtml/VChartHTML.html (accessed: April 2022).